Engineering Fracture Mechanics 267 (2022) 108427

Contents lists available at ScienceDirect

Engineering Fracture Mechanics

journal homepage: www.elsevier.com/locate/engfracmech

A stabilized mixed-FE scheme for frictional contact and shear failure analyses in deformable fractured media

Luyu Wang [a,b,*], Cornelis Vuik [a], Hadi Hajibeygi [b]

[a] Department of Applied Mathematics, Delft University of Technology, 2628 CD Delft, The Netherlands
[b] Department of Geoscience and Engineering, Delft University of Technology, 2628 CV, Delft, The Netherlands

ARTICLE INFO

Keywords:
Fractured media
Frictional contact
Crossing fractures
Lagrange multipliers
Mixed-finite element method

ABSTRACT

Simulation of fracture contact mechanics in deformable fractured media is of paramount important in computational mechanics. Previous studies have revealed that compressive loading may produce mode II fractures, which is quite different from mode I fractures induced by tensile loading. Furthermore, fractures can cross each other. This will increase the complexity of their network deformation under different loading types significantly. In this work, a stabilized mixed-finite element (FE) scheme with Lagrange multipliers is proposed in the framework of variational formulation, which is able to simulate frictional contact, shear failure (mode II) and opening (mode I) of multiple crossing fractures. A novel treatment is devised to guarantee physical solutions at the intersection of crossing fractures. A preconditioner is introduced to re-scale the saddle-point algebraic system and to preserve the numerical robustness. Then, a solution strategy is designed to calculate the unknowns, displacement and Lagrange multipliers, in one algebraic system. Later, numerical tests are conducted to study mechanical behaviors of fractured media. Benchmark study is performed to verify the presented mixed-FE scheme. A deformable medium with crossing fractures is simulated under mixed-mode loading types. The characteristics of fracture contact, surface sliding, opening and variation of stress intensity factor are analyzed. Simulation results show that the curve of slippage induced by compression, as well as the opening induced by internal fluid pressure, along the fracture length holds a parabolic shape. The diagonal contact point, at the intersecting position of the crossing fractures, is studied in detail, specially under different stress states. Finally, the impact of intersecting fractures on frictional contact mechanics is investigated for different loading conditions.

1. Introduction

The subject of computational contact mechanics is a pillar in applied and computational mechanics [1,2]. Especially, it plays an essential role in geoscience applications, such as reservoir engineering, subsurface energy exploration and faults activation [3–5]. Discrete fractures widely exist in geological fields with significantly contrasting hydraulic and mechanical properties [6,7]. The formation of the fracture networks and their evolution depend on the loading condition imposed by the surrounding geological environment [8–10]. Moreover, the multiple crossing fractures lead to several complicated mechanical behaviors, specially when the fractures are subjected to compressive loading (mode II fracture). In this context, the two sides of fracture plane contact and interact with each other, which produce contact tractions. It is totally different from the scenario of tensile loading (mode I fracture), as in the situation of hydraulic-driven fractures, in which the contact constraints disappear as the two sides of the fractures are

* Correspondence to: GeoRessources Lab., UMR 7359, CNRS, 54500 Vandœuvre-lès-Nancy, France.
E-mail addresses: wang.luyu@cnrs.fr (L. Wang), c.vuik@tudelft.nl (C. Vuik), h.hajibeygi@tudelft.nl (H. Hajibeygi).

https://doi.org/10.1016/j.engfracmech.2022.108427
Received 17 November 2021; Received in revised form 24 March 2022; Accepted 26 March 2022
Available online 4 April 2022

separate [11,12]. However, several challenges appear in the situation of crossing fractures [13], in which proper treatments at the intersection of crossing fractures need more attentions.

The classical computational contact mechanics mainly studies the contact between two separate deformable (or rigid) bodies [14–17]. In contrast to this, geoscience applications often include deformable porous media which entail several fractures [18–20]. Furthermore, these discrete fractures are characterized with multiple contact surfaces. This configuration is unusual in classical contact mechanics but quite common in geoscience applications [21].

To this end, the classical contact mechanics theory is extended to the category of fault mechanics [3–5,18,19], with the aim to mainly model the slip and contact traction on mode II fractures. On the other hand, to simplify the computational workflow, sometimes the explicit treatment of contact mechanics is neglected [20]. This simplification is feasible in case of hydro-fracturing problem, when the mode I fractures are under tensile stress [11,12]. For compressive stress, however, such simplifications lead to significant errors. The particular interest is to develop a computational model which allows for explicit consideration of both opening and slippage (i.e. normal and tangential displacements). In this work, we consider the frictional contact mechanics and surface sliding by Lagrange multipliers, in which both the slippage and opening of fracture can be accurately simulated.

In the numerical methods based on continuum mechanics, the category of mesh-based methods is developed and improved to model the frictional contact and sliding. Among these methods, finite element method (FEM) is the most widely used method in computational contact mechanics [2–5,15,16]. Recently, the extended finite element method (XFEM) [22–24] and finite volume method (FVM) [25–27] have been proposed to simulate frictional contact in fractured media. However, the classical contact mechanics studies the single contact surface. Based on this, the numerical methods for multiple interfaces in fractured media have been proposed. In the aspect of treatment of contact constraints, the penalty method [28,29] and the Lagrange multiplier method [30,31] are the two main schemes originated from the variational principle. Meanwhile, numerical schemes with variationally consistent hybrid formulation have been also proposed [25], in which the multi-point stress approximation [32] was used to discretize the governing equations. Note that XFEM has been developed by the penalty method [23] and Lagrange multiplier method [22] to model frictional contact on fracture.

The drawback of penalty method is that the resulted algebraic system could be ill-conditioned. The key point is to apply (elastic) springs to connect the two sides of the contact surfaces. This approach is inaccurate, since it enforces springs with large stiffness coefficients [28,29]. The Lagrange multiplier method, however, introduces an additional unknown [31,33], namely the Lagrange multiplier. It has an underlying physical meaning, i.e., the contact tractions on fracture surface. The inconvenience is the additional cost of solving the augmented algebraic system with the so-called saddle-point structure [34–36]. More precisely, the Lagrange multiplier method results in the mixed-FE scheme [34,37], in which the displacement and Lagrange multiplier can be calculated at one single global algebraic block. Other methods, such as the Nitsche's method [38,39], augmented Lagrange multiplier method [31,40] and mortar method [41,42] have been also proposed. Recently, the Nitsche method has been applied to address contact mechanics in the thermo-hyro-mechanical processes [43]. Based on the remeshing techniques, the fracture propagation is also studied [44,45], which is then extended to a multiscale simulation framework [46]. In fact, most of these methods are based on the basic principles of penalty method and Lagrange multiplier method, within the framework of variational principle. The highly nonlinear property of the contact system is captured by the so-called Karush–Kuhn–Tucker (KKT) condition [1,2,14–16], which is integrated into the standard variational principle, resulting in the constrained variational principle. The prospective directions on computational contact mechanics is focused on the treatment of multiple fractured media, including crossing fractures, and development of stable [34,36,47] and scalable iterative solvers [34] for the resulting saddle-point systems. Such developments would allow for modeling large-scale systems within the industrial applications.

Despite being crucially important, the accurate and stable modeling of multiple crossing fractured media remains to a large extend unexplored. This work develops a novel approach to resolve this limitation. The FE-based system on an unstructured mesh is developed in which fractures are confined at the matrix element interfaces. Then, a constraint is introduced to guarantee physical solutions in presence of crossing fractures. The potential contact pairs are defined to resolve the contact mechanics at the intersected position. The resulting system contains displacement unknowns and Lagrange multipliers, leading to the saddle-point structure. We develop a scaling algorithm to improve the system condition number and thus leads to a robust solution strategy. The developed method is being benchmarked against analytical methods, and tested for several proof-of-concept numerical test cases.

This paper is structured as follows. First, the formulation of frictional contact and shear failure on multiple crossing fractures is presented in Section 2. Then, the contact constraints are integrated into variational principle using Lagrange multiplier. Galerkin FE approximation is applied in Section 3 to discretize the system. In Section 4, a solution strategy is proposed with the devised monolithic-updated contact algorithm, in which the preconditioning is used to preserve the robustness of the saddle-point system. Finally, a series of numerical tests is performed in Section 5 to verify the proposed method and to analyze the mechanical behaviors of deformable fractured media.

2. Physical model

The formulation is presented after a revisit on the theory of contact mechanics. Both the isolated fracture and crossing fractures can be simulated in this framework. The compressive state would lead to the activation of contact constraints, while the tensile state remains the standard scheme of elasticity.

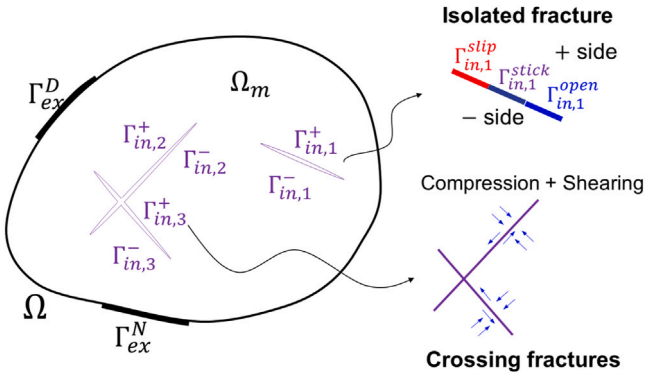

Fig. 1. Schematic of a deformable medium with multiple fractures. Each fracture is decomposed into a positive and a negative surfaces.

2.1. Model of deformable media with crossing fractures

The porous medium is denoted as Ω^m. As shown in Fig. 1, a set of the discrete fractures ω is distributed in the domain and is modeled as the internal boundaries Γ_{in} inside Ω^m. Each of the fracture surfaces is decomposed into the positive side Γ_{in}^+ and the negative side Γ_{in}^-, such that $\Gamma_{in} = \Gamma_{in}^+ \cup \Gamma_{in}^-$. For multiple fractures, it reads:

$$\omega := \Gamma_{in} = \sum_{i=1}^{N^f} \Gamma_{in,i} = \sum_{i=1}^{N^f} \left(\Gamma_{in,i}^+ \cup \Gamma_{in,i}^- \right) \tag{1}$$

where N^f is the number of fractures. According to the convention in computational contact mechanics [2,14–16], we also adopt the terms of master surface Γ_{in}^- and slave surface Γ_{in}^+.

The external boundary Γ_{ex} is expressed by $\Gamma_{ex} = \Gamma_{ex}^D \cup \Gamma_{ex}^N$ and $\Gamma_{ex}^D \cap \Gamma_{ex}^N = \emptyset$, with Dirichlet- and Neumann-boundaries, namely Γ_{ex}^D and Γ_{ex}^N. The domain Ω can be decomposed into $\Omega = \Omega^m \cup \Gamma_{in}$, with the boundaries of external- and internal-types $\partial\Omega = \Gamma_{ex} \cup \Gamma_{in}$.

One of the novelties in this work is to model the contact behavior and sliding of Γ_{in}. The constraint on fracture surfaces depends on the type of loading as well as the frictional law, which controls the sliding (mode II) or opening (mode I) of fractures. Especially, the Karush–Kuhn–Tucker (KKT) condition [1,2,14,15] would be active once the contact surface is imposed by compression. It is used to confine the unphysical effects of surface penetration and mesh overlapping, as displayed in Fig. 2. The details of contact constraints will be introduced in Section 2.3.

2.2. Governing equations

The host matrix is assumed as an elastic medium. The assumptions of infinitesimal deformation and the quasi-static contact are employed. The deformation of Ω is captured by the momentum balance combining with Hooke's law:

$$\nabla \cdot (\mathbb{C} : \nabla^s \mathbf{u}) + \mathbf{f} = \mathbf{0} \quad \text{on } \Omega \tag{2}$$

with the body force $\mathbf{f}$ and elasticity tensor $\mathbb{C}$. $\mathbf{u}$ is the displacement vector, ∇^s the symmetric gradient.

It is straightforward to define boundary conditions for the external boundary. The pre-defined displacement $\bar{\mathbf{u}}^{ex}$ and traction $\bar{\mathbf{t}}^{ex}$ are given as:

$$\begin{aligned} \mathbf{u} &= \bar{\mathbf{u}}^{ex} \quad \text{on } \Gamma_{ex}^D \\ \boldsymbol{\sigma} \cdot \mathbf{n}^{ex} &= \bar{\mathbf{t}}^{ex} \quad \text{on } \Gamma_{ex}^N \end{aligned} \tag{3}$$

with the outward unit vector $\mathbf{n}^{ex}$ which points outward of the external boundary.

The situation is totally different once fractures are introduced. Providing a reasonable and correct condition is complicated for Γ_{in} (also known as the fractures) because of the nonlinear constraints on fractures [2,14]. The system of nonlinear inequalities (the KKT condition) [2,15] are introduced:

$$\mathbf{C}\left(\mathbf{u}^f, \mathbf{t}^f\right) \geqslant \mathbf{0} \quad \text{on } \Gamma_{in} \tag{4}$$

with the displacement $\mathbf{u}^f$ and traction $\mathbf{t}^f$ on the contact surface. The expanded form will be introduced in Section 2.3.

The external boundary condition Eq. (3) is allowed to be compressive or tensile. The later case can be treated easily by the standard finite element framework. The fracture surfaces exhibit complex behaviors if compression is applied, as shown in Fig. 2.

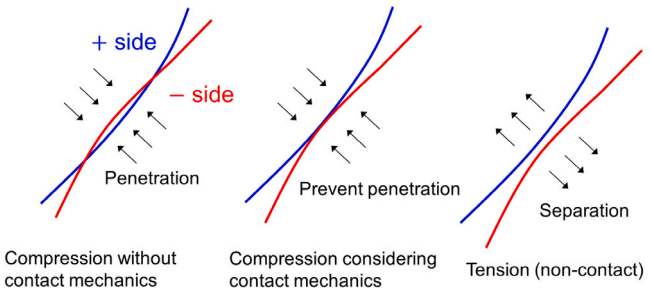

Fig. 2. Fracture states under different loading conditions. The contact constraints are activated in compression and disappears under tension.

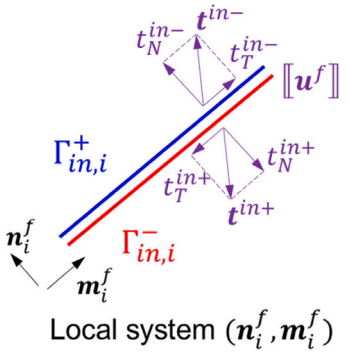

Fig. 3. The local system attached to a fracture surface.

2.3. Constraints on local system of fractures

The system of additional constraint equations Eq. (4) on fractures is taken as a complement of the standard boundary condition Eq. (3). Generally speaking, as shown in Fig. 1, a certain fracture can be slip, stick or open. Furthermore, the contact surface is divided into several portions $\Gamma_{in} = \Gamma_{in}^{stick} \cup \Gamma_{in}^{slip} \cup \Gamma_{in}^{open}$.

The local coordinate system $(\mathbf{n}^f, \mathbf{m}^f)$, defined by the unit-normal vector $\mathbf{n}^f$ and the unit-tangential vector $\mathbf{m}^f$, is attached to each of fractures, as shown in Fig. 3. To define the sign of $\mathbf{n}^f$, we classify the positive and negative vectors, $\mathbf{n}^+$ and $\mathbf{n}^-$, for the two sides Γ_{in}^+ and Γ_{in}^-, respectively. The default directions of unit vector and traction used in the presented numerical scheme are defined:

$$\mathbf{n}^f = \mathbf{n}^- = -\mathbf{n}^+ \quad \text{and} \quad \mathbf{t}_N^f = \mathbf{t}_N^{in-} = -\mathbf{t}_N^{in+} \tag{5}$$

where $\mathbf{n}^f$ is a vector that points from the negative side to the positive side. $\mathbf{t}_N^{in\pm}$ is the normal component of contact traction on $\pm$ sides.

The unit vector $\mathbf{n}^f$ is used to define the normal component of a local system. We adopt the assumption of infinitesimal deformation, therefore $\mathbf{n}^f$ is directly defined in the initial configuration. The normal traction of contact $\mathbf{t}_N^f$ is calculated by stress tensor $\boldsymbol{\sigma}$ based on the traction vector $\mathbf{t}^f$, which is given by:

$$\mathbf{t}^f = \boldsymbol{\sigma} \cdot \mathbf{n}^f = t_N^f \mathbf{n}^f + t_T^f \mathbf{m}^f \tag{6}$$

where the sign of compression is negative, vise versa.

Fig. 3 depicts a local coordinate system $(\mathbf{n}^f, \mathbf{m}^f)$ for a certain fracture. The quantity $[\![\mathbf{u}^f]\!]$ on a contact surface is introduced to evaluate the relative deformation between the two sides Γ_{in}^+ and Γ_{in}^-:

$$[\![\mathbf{u}^f]\!] = \mathbf{u}^{f+} - \mathbf{u}^{f-} \tag{7}$$

with the absolute displacements $\mathbf{u}^{f+}$ and $\mathbf{u}^{f-}$ on two sides of the contact surface. The two components of relative displacement are defined as:

$$[\![u_N^f]\!] = [\![\mathbf{u}^f]\!] \cdot \mathbf{n}^f \quad \text{and} \quad [\![u_T^f]\!] = [\![\mathbf{u}^f]\!] \cdot \mathbf{m}^f \tag{8}$$

Therefore, the additional constraint conditions are used to confine the mechanical behavior of contact surface on the normal direction:

$$\begin{aligned} g_N &= [\![u_N^f]\!] \geqslant 0 \quad \text{on } \Gamma_{in} \\ t_N^f &\leqslant 0 \quad \text{on } \Gamma_{in} \\ g_N t_N^f &= 0 \quad \text{on } \Gamma_{in} \end{aligned} \tag{9}$$

and the tangential direction:

$$\begin{aligned} \tau_c &= c - t_N^f \tan\varphi \quad \text{on } \Gamma_{in} \\ t_T^f &= \tau_c \frac{[\![u_T^f]\!]}{\|[\![u_T^f]\!]\|_2} \quad \text{on } \Gamma_{in} \end{aligned} \tag{10}$$

where symbol $\|\cdot\|_2$ is the 2-norm. The critical value of τ_c is determined by Mohr–Coulomb criterion. c and φ are parameters to control frictional behavior. The sign of t_T^f is of great important to calculate the dissipate energy induced by contact friction. In this work, we employ the so-called maximum plastic dissipate principle [15,18,48] to obtain the direction of t_T^f, in which $[\![u_T^f]\!]$ is the weighted quantity.

Eqs. (9) and (10) are the expanded forms of Eq. (4), which hold true on contact surface of each fracture. They provide a set of constraint equations to define the frictional contact, which are considered as requisite complements to Eqs. (2) and (3).

3. Numerical discretization

The constraints of frictional contact are integrated in the mixed-finite element scheme through Lagrange multipliers. Then, the Galerkin finite element approximation is used to derive the fully discretized scheme then resulting an unified computational formula.

3.1. Variational formulation of deformable media with multiple fractures

In this section, the standard variational principle is extended to include the contact mechanics and sliding of multiple fractures. Note that Eq. (10) is inactive if the current traction component t_T^f is lower than the critical traction τ_c.

We use the Galerkin finite element formulation (GFEM) [15,49] to integrate the contact constraints Eqs. (9) and (10). The standard variational principle (SVP) is extended to a more general case. According to the Lagrange multiplier method [49–51], SVP is generalized to the constrained variational principle (CVP). The total energy functional is introduced as:

$$\Pi^*\left(\mathbf{u}, \mathbf{u}^f, \lambda\right) = \Pi_u\left(\mathbf{u}\right) + \Pi^{CL}\left(\mathbf{u}^f, \lambda\right) \tag{11}$$

with the elastic functional $\Pi_u(\mathbf{u})$ defined by SVP, which is related to the unknown (displacement $\mathbf{u}$). The novelty is the contact functional $\Pi^{CL}\left(\mathbf{u}^f, \lambda\right)$ defined by CVP through Lagrange multiplier λ.

The Lagrange multiplier vector reveals an underlying meaning in physical aspect. The component form $\lambda = \begin{bmatrix}\lambda_N & \lambda_T\end{bmatrix}^T$ indicates that it equals the components of contact traction on the surface. To solve the system, the first-order variation of Eq. (11) is written as:

$$\delta\Pi^*\left(\mathbf{u}, \mathbf{u}^f, \lambda\right) = \underbrace{\delta\Pi_u\left(\mathbf{u}\right)}_{\text{Elasticity}} + \underbrace{\delta\Pi_u^{CL}\left(\mathbf{u}^f, \lambda\right) + \delta\Pi_\lambda^{CL}\left(\mathbf{u}^f, \lambda\right)}_{\text{Frictional contact and slip}} \tag{12}$$

The last two terms in right-hand side of Eq. (12) are induced by the effects from frictional contact and sliding. The Lagrange multiplier method provides a way to integrate contact constraints with the help of Eqs. (2), (3) and (4):

$$\begin{aligned} \delta\Pi^*\left(\mathbf{u}, \mathbf{u}^f, \lambda\right) = & \underbrace{\int_\Omega \delta\boldsymbol{\varepsilon}^T \boldsymbol{\sigma} d\Omega - \int_\Omega \delta\mathbf{u}^T \mathbf{f} d\Omega - \int_{\Gamma_{ex}^N} \delta\mathbf{u}^T \bar{\mathbf{t}}^{ex} d\Gamma}_{\text{Induced by elastic deformation of the matrix}} \\ & + \underbrace{\sum_{i=1}^{N^f} \left(\int_{\Gamma_{in,i}} \delta\lambda^T \mathbf{C}\left(\mathbf{u}^f, \mathbf{t}^f\right) d\Gamma + \int_{\Gamma_{in,i}} \lambda^T \delta\mathbf{C}\left(\mathbf{u}^f, \mathbf{t}^f\right) d\Gamma \right)}_{\text{Induced by frictional contact and slip on fractures}} \end{aligned} \tag{13}$$

The constrained variational principle requires $\delta\Pi^*\left(\mathbf{u}, \mathbf{u}^f, \lambda\right) = 0$ with respect to displacement $\mathbf{u}$:

$$\int_\Omega \delta\boldsymbol{\varepsilon}^T \boldsymbol{\sigma} d\Omega - \int_\Omega \delta\mathbf{u}^T \mathbf{f} d\Omega - \int_{\Gamma_{ex}^N} \delta\mathbf{u}^T \bar{\mathbf{t}}^{ex} d\Gamma + \sum_{i=1}^{N^f} \int_{\Gamma_{in,i}} \lambda^T \delta\mathbf{C}\left(\mathbf{u}^f, \mathbf{t}^f\right) d\Gamma = 0 \tag{14}$$

and with respect to Lagrange multiplier λ:

$$\sum_{i=1}^{N^f} \int_{\Gamma_{in,i}} \delta\lambda^T \mathbf{C}\left(\mathbf{u}^f, \mathbf{t}^f\right) d\Gamma = 0 \tag{15}$$

with the number of fractures N^f. The situation of multiple fractures is then included.

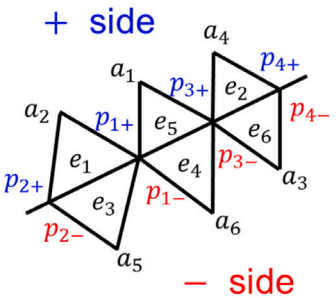

Node		
1	a_2	−1
2	p_{2+}	1
3	p_{1+}	1
4	a_1	−1
5	p_{3+}	1
6	a_4	−1
7	p_{4+}	1
8	a_5	−1
9	p_{2-}	1
10	p_{1-}	1
11	p_{3-}	1
12	a_6	−1
13	a_3	−1
14	p_{4-}	1

Contact pairs				
1	p_{1+}	p_{1-}	$n^f_{p_1}$	$g_{N_{p_1}}$
2	p_{2+}	p_{2-}	$n^f_{p_2}$	$g_{N_{p_2}}$
3	p_{3+}	p_{3-}	$n^f_{p_3}$	$g_{N_{p_3}}$
4	p_{4+}	p_{4-}	$n^f_{p_4}$	$g_{N_{p_4}}$

Note: notation of non-contact nodes (-1) and contact nodes (1).

Fig. 4. Definition of contact pairs in a local system on the unstructured grids.

3.2. Galerkin finite element approximations

The first three terms in Eq. (14) can be easily treated by the standard Galerkin finite element method. The key point is the fourth term at the left-hand side, which describes the effects from contact and sliding.

The sliding on fracture will occur if the tangential contact traction reaches the critical value τ_c, as indicated in Eq. (10). In this context, the tangential component is obtained by Mohr–Coulomb criterion, which means $\lambda_T = \tau_c$. We define the indicator function for slip contact:

$$sign = \frac{[\![u_T^f]\!]}{\|[\![u_T^f]\!]\|_2} = \begin{cases} 1 & \text{slip along direction of } \mathbf{m}^f \\ -1 & \text{slip along direction of } -\mathbf{m}^f \end{cases} \tag{16}$$

Consequently, the component λ_T of unknown λ is expressed by $\lambda_T = \left(c - \lambda_N \tan\varphi\right) sign$. In this way, λ_T is connected to the unknown λ_N. Fracture sliding occurs if Eqs. (9) and (10) are active (mode II). In contrast, if the contact surface is subjected to tension (mode I), the contact constraints are disappeared. Then, the formulation would be reduced to the SVP framework, which can be expressed by the first three terms at right-hand side of Eq. (13).

Therefore, the weak forms of the governing equations can be obtained. We refer to Appendix A for the detail.

The governing equations can be fully discretized using Galerkin finite element method [15,49]. As the requirement of finite element method, the solutions λ and $\mathbf{u}$ are subjected to the square integrable functional spaces [34,52,53]. The finite element approximations are given as:

$$\begin{aligned} \mathbf{u} \approx \mathbf{u}_h &= \sum_{i=1}^{n_{node}} \mathbf{N}_i^u \mathbf{U}_i = \mathbf{N}^u \mathbf{U} \\ \lambda \approx \lambda_h &= \sum_{j=1}^{n_{cp}} \mathbf{N}_j^\lambda \boldsymbol{\Lambda}_j = \mathbf{N}^\lambda \boldsymbol{\Lambda} \end{aligned} \tag{17}$$

with displacement vector $\mathbf{U}$ and Lagrange multiplier vector $\boldsymbol{\Lambda}$ at grid vertices, and the shape function matrices $\mathbf{N}^u$ and $\mathbf{N}^\lambda$. Note that the numbers of nodes and contact pairs are denoted by n_{node} and n_{cp}.

The relative displacement between + side and — side is measured by the jump displacement vector $[\![\mathbf{u}^f]\!]$ in local system, as shown in Fig. 4. The transformation matrix $\mathbf{G}$ achieves the expression of relative displacement on fracture surface. To convert the quantity from global system to local system, the rotation matrix $\mathbf{S}$ is defined by unit vectors of the local system. Consequently, the jump displacement reads:

$$[\![\hat{\mathbf{u}}^f]\!] = \mathbf{S}^T \mathbf{G} \mathbf{U}^f \tag{18}$$

with the displacement vector $\mathbf{U}^f$ related to the fracture surface. Strain $\boldsymbol{\epsilon}$ and stress $\boldsymbol{\sigma}$ are expressed as:

$$\boldsymbol{\epsilon} = \mathbf{B}\mathbf{U} \quad \text{and} \quad \boldsymbol{\sigma} = \mathbf{D}\mathbf{B}\mathbf{U} \tag{19}$$

with the elastic matrix $\mathbf{D}$ and the strain operator $\mathbf{B}$.

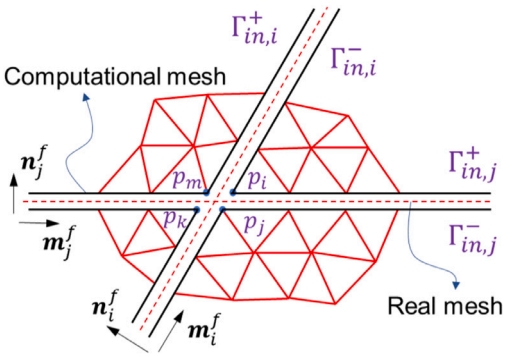

Fig. 5. Schematic of contact pairs on crossing fractures.

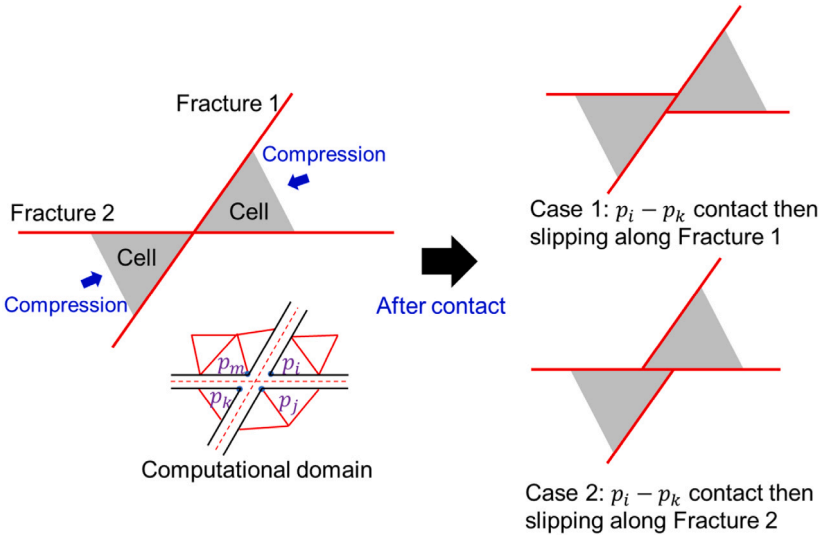

Fig. 6. Illustration of diagonal contact at the intersected position.

It is straightforward that the discretized forms can be obtained once substituting the quantities in weak forms using the expressions Eqs. (17), (18) and (19):

$$\begin{aligned}\int_{\Omega}\delta\mathbf{U}^T\mathbf{B}^T\mathbf{D}\mathbf{B}\mathbf{U}d\Omega-\int_{\Omega}\delta\mathbf{U}^T\left[\mathbf{N}^u\right]^T\mathbf{f}d\Omega-\int_{\Gamma_{ex}^N}\delta\mathbf{U}^T\left[\mathbf{N}^u\right]^T\bar{\mathbf{t}}^{ex}d\Gamma\\+\sum_{i=1}^{N^f}\int_{\Gamma_{in,i}}\delta\mathbf{U}^T\mathbf{G}^T\mathbf{S}\mathbf{N}^{\lambda}\boldsymbol{\Lambda}d\Gamma=0\\\sum_{i=1}^{N^f}\int_{\Gamma_{in,i}}\delta\boldsymbol{\Lambda}^T\left[\mathbf{N}^{\lambda}\right]^T\mathbf{S}^T\mathbf{G}\mathbf{U}d\Gamma=-\sum_{i=1}^{N^f}\int_{\Gamma_{in,i}}\delta\boldsymbol{\Lambda}^T\left[\mathbf{N}^{\lambda}\right]^T\mathbf{g}d\Gamma\end{aligned}\tag{20}$$

In the situation of fracture sliding, the tangential component which related to $\boldsymbol{\Lambda}$ in Eq. (20) needs to be replaced by the critical traction τ_c defined in Eq. (10). Meanwhile, it is important that employing Eq. (16) to determine the direction of slip contact.

Before introduce the solution strategy, the treatment of contact and sliding on crossing fractures is addressed in Section 3.3.

3.3. A novel treatment of contact on crossing fractures

Normally, in classical computational contact mechanics, the concept of contact pair is used to capture the contact or impact between two separate deformable (or rigid) bodies, in which the situation of crossing contact surfaces is unusual, see [15–17]. In contrast to that, it is very common in geoscience applications that discrete fractures would cross each other, so that the contact mechanics of crossing fractures should be addressed.

Fig. 5 shows a schematic of crossing fractures and their contact pairs defined in the local systems of fractures $\Gamma_{in,i}$ and $\Gamma_{in,j}$. The hybrid-dimensional modeling approach is applied to generate the grids of the matrix and the fractures [7,9]. The node-split

technique [3,5,44] is applied to duplicate the nodes on contact surface, so that the computational mesh allows a relative displacement on the position of crossing fractures. For example, four points p_i, p_j, p_k, p_m are defined on the crossing position. They would be contacted if fracture $\Gamma_{in,i}$ (or fracture $\Gamma_{in,j}$) is imposed by compression. To capture this interaction, the "crossing contact pairs" are devised in the presented numerical scheme. Particularly, the diagonal contact should be considered. Assuming the + and — sides of surface $\Gamma_{in,i}$ would be in contact, the crossing contact pairs $p_i - p_m$, $p_i - p_k$, $p_j - p_m$ and $p_j - p_k$ are constructed. Similarly, for the surface $\Gamma_{in,j}$, the crossing contact pairs are $p_i - p_j$, $p_i - p_k$, $p_m - p_k$ and $p_m - p_j$, in which $p_i - p_k$ and $p_m - p_j$ are the diagonal contact pairs. If compressive loading is not active, the crossing contact pairs allow to be separated.

Furthermore, the potential scenarios are illustrated in Fig. 6. The diagonal contact would be occurred if the contact pairs along the diagonal are activated. Fig. 6 shows a potential diagonal contact, where the crossing contact pair $p_i - p_k$ is activated. Depending on the stress state, the two diagonal nodes may slip along either Fracture 1 or Fracture 2. Therefore, to analyze the potential diagonal contacts, numerical tests are performed with different loading directions under compression and tension, as discussed in Section 5.4.

4. Solution strategy of the stabilized mixed-FE scheme

In this section, the algebraic form of the contact system is derived and resulting an unified matrix formulation. The system of contact mechanics is solved by iteration method. The preconditioner is introduced to handle the saddle-point algebraic system. It leads to a preconditioned mixed-FE scheme. All algorithms are implemented in our C++ code.

4.1. The iteration method for contact mechanics

The system of contact mechanics is a nonlinear system, where the unknowns $\mathbf{U}$ and $\boldsymbol{\Lambda}$ are coupled together. As shown in system Eq. (20), the two equations depend on each other. Consequently, the mixed-finite element formulation [34,35,37] is formulated. In this way, the two primary unknowns can be calculated by one non-linear system in a monolithic strategy. Residual vector $\mathbf{R} = [\mathbf{R}^u \quad \mathbf{R}^\lambda]^T$ is constructed for the iteration. The superscripts u and λ mean the displacement and Lagrange multiplier. In the iteration, we wish the L^2-norm of residual vector converges to zero:

$$\lim_{n\to\infty} \|\mathbf{R}^n\|_2 = \mathbf{0} \tag{21}$$

where the components of residual vector $\mathbf{R}$ are defined based on Eq. (20):

$$\begin{aligned}\mathbf{R}^u = &\int_\Omega \delta\mathbf{U}^T\mathbf{B}^T\mathbf{D}\mathbf{B}\mathbf{U}d\Omega - \int_\Omega \delta\mathbf{U}^T\left[\mathbf{N}^u\right]^T\mathbf{f}d\Omega - \int_{\Gamma_{ex}^N}\delta\mathbf{U}^T\left[\mathbf{N}^u\right]^T\bar{\mathbf{t}}^{ex}d\Gamma \\ &- \sum_{i=1}^{N^f}\int_{\Gamma_{in,i}}\delta\mathbf{U}^T\mathbf{G}^T\mathbf{S}\mathbf{N}^\lambda\boldsymbol{\Lambda}d\Gamma \\ \mathbf{R}^\lambda = &\sum_{i=1}^{N^f}\int_{\Gamma_{in,i}}\delta\boldsymbol{\Lambda}^T\left[\mathbf{N}^\lambda\right]^T\mathbf{S}^T\mathbf{G}\mathbf{U}d\Gamma + \sum_{i=1}^{N^f}\int_{\Gamma_{in,i}}\delta\boldsymbol{\Lambda}^T\left[\mathbf{N}^\lambda\right]^T\mathbf{g}d\Gamma\end{aligned} \tag{22}$$

Then, the Newton–Raphson iteration method is introduced to linearize the nonlinear system. Jacobian $\mathbf{J}^\nu$ and residual vector $\mathbf{R}^\nu$ should be calculated at each iteration step ν. The unknown vector $\mathbf{x} = [\mathbf{U} \quad \boldsymbol{\Lambda}]^T$ can be solved at step $\nu+1$ in incremental form $\delta\mathbf{x}^{\nu+1}$:

$$\begin{bmatrix}\mathbf{J}_{11} & \mathbf{J}_{12}\\ \mathbf{J}_{21} & \mathbf{J}_{22}\end{bmatrix}^\nu\begin{bmatrix}\delta\mathbf{U}\\ \delta\boldsymbol{\Lambda}\end{bmatrix}^{\nu+1} = -\begin{bmatrix}\mathbf{R}^u\\ \mathbf{R}^\lambda\end{bmatrix}^\nu \tag{23}$$

with the components of Jacobian $\mathbf{J}_{ij}$ $(i,j=1,2)$, which are determined by the derivative of residual vector with respect to unknown vector:

$$\mathbf{J}^\nu = \frac{\partial\mathbf{R}}{\partial\mathbf{x}}|^\nu \tag{24}$$

The contact system can be then written as the algebraic form based on Eqs. (23) and (24):

$$\begin{bmatrix}\mathbf{K}^{uu} & \mathbf{C}^{\lambda u}\\ \left[\mathbf{C}^{\lambda u}\right]^T & \mathbf{0}\end{bmatrix}\begin{bmatrix}\delta\mathbf{U}\\ \delta\boldsymbol{\Lambda}\end{bmatrix} = -\begin{bmatrix}\mathbf{R}^u\\ \mathbf{R}^\lambda\end{bmatrix} \tag{25}$$

where the effects induced by slip and stick could be reflected through block $\mathbf{C}^{\lambda u}$ and its transpose $\left[\mathbf{C}^{\lambda u}\right]^T$. $\mathbf{K}^{uu}$ is the block related to displacement. The components in Eq. (25) are provided in Appendix B.

4.2. Preconditioning of the saddle-point algebraic system

It should be noted that the lower block diagonal entry of the Jacobian in Eq. (25) is a zero matrix. The shape of $\mathbf{C}^{\lambda u}$ is rectangular, while $\mathbf{K}^{uu}$ is a square matrix, as shown in Fig. 7. These features lead to a special algebraic structure, which is the so-called saddle-point system [34–36]. Furthermore, the ill-condition Jacobian $\mathbf{J}$, which has a high condition number, would lead to a numerical instability when solving the saddle-point system Eq. (25). To this end, the preconditioning technique is presented to improve the numerical robustness of the system.

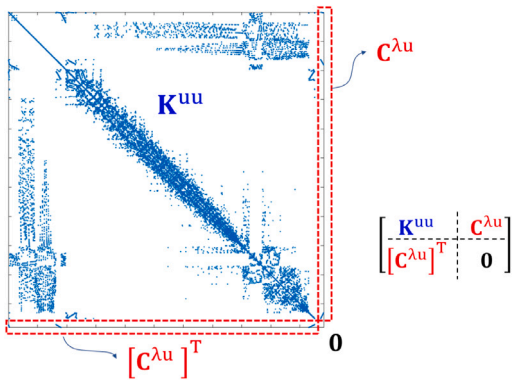

Fig. 7. The pattern of non-zero entries of saddle-point system resulted by the presented numerical scheme.

The preconditioned Jacobian $\bar{\mathbf{J}}$ with a low condition number is derived through the preconditioned operation:

$$\bar{\mathbf{J}} = \mathbf{PJ} = \begin{bmatrix} \mathbf{A}^{-1} & \mathbf{0} \\ \mathbf{0} & \mathbf{B}^{-1} \end{bmatrix} \begin{bmatrix} \mathbf{K}^{uu} & \mathbf{C}^{\lambda u} \\ [\mathbf{C}^{\lambda u}]^T & \mathbf{0} \end{bmatrix} \tag{26}$$

with the components $\mathbf{A}$ and $\mathbf{B}$ of preconditioner $\mathbf{P}$. They are defined by the norms of $\mathbf{K}^{uu}$ and $\mathbf{C}^{\lambda u}$. For convenience, we denote $[\mathbf{C}^{\lambda u}]^T = \mathbf{D}$ and $[\mathbf{K}^{uu} \ \ \mathbf{C}^{\lambda u}] = \mathbf{E}$. We refer to C for the expanded forms.

Combining the system of Eqs. (25), (B.1), (B.2) with the operation Eq. (26), a preconditioned mixed-FE scheme is presented, which is one of the core innovations in the presented work. The attractive feature is ease of implementation and it can be directly integrated into an existing solver.

4.3. Global strategy: the monolithic-updated contact algorithm

The contact system should be resolved using an iteration strategy, since the governing equations of contact mechanics are a set of nonlinear partial differential equations. Moreover, the contact state of each contact pair should be updated dynamically at each time step and depends on the loading condition. It is essential that to check the contact state based on the contact constrained conditions and current stress/displacement condition. Meanwhile, each of the contact pairs should be evaluated at each iteration. To this end, the monolithic-updated contact algorithm is designed to update the unknowns (displacement and Lagrange multiplier) in one algebraic system, as shown in Appendix D.

5. Numerical results and discussion

In this section, a series of numerical tests is conducted to study the frictional contact and sliding of single- and multi-crossed fractures based on the proposed mixed-FE scheme. First, a benchmark study is presented to verify the numerical scheme. Later, the contact behavior on single fracture is studied under mixed-mode loading. Finally, tests with complex geometry are studied. The slippage and opening of fractures are analyzed under different conditions.

5.1. Fracture slip controlled by frictional law

A fractured medium, which contains a single inclined fracture with angle α and length $2l$, is modeled when the uniaxial loading σ_∞ is imposed. As shown in Fig. 8, the numerical model is constructed and two patterns with different inclined angles are considered. We adopt the assumptions of homogeneous and linear elastic material with Young's modulus $E = 25$GPa and Poisson ratio $\nu = 0.25$. The parameters of frictional law are frictional angle $\varphi = 30°$ and cohesion $c = 0$. Note that the compression $\sigma_\infty = 10$ MPa and crack length $2l = 2$ m.

This model is selected as a benchmark test to verify the proposed numerical method. To this end, the slippage (i.e. the relative tangential displacement) on contact surface can be calculated by the analytical solution from literature [54]:

$$[\![u_T^f]\!] = \frac{4t_T^f\left(1-\nu^2\right)}{E}\sqrt{l^2-(\eta-l)^2} \tag{27}$$

with the tangential and normal components of contact traction:

$$\begin{aligned} t_T^f &= \sigma_\infty \sin\alpha\cos\alpha - \sigma_\infty \sin^2\alpha\tan\varphi \\ t_N^f &= -\sigma_\infty \sin^2\alpha \end{aligned} \tag{28}$$

where $0 \leqslant \eta \leqslant 2l$ is the coordinate along the length of contact surface.

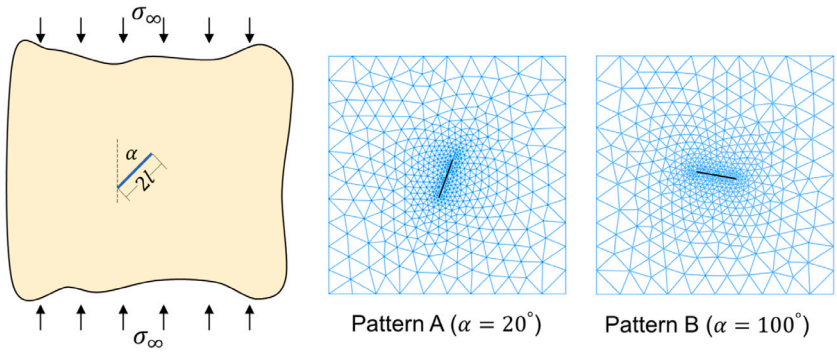

Fig. 8. Schematic of a deformable medium with a single fracture.

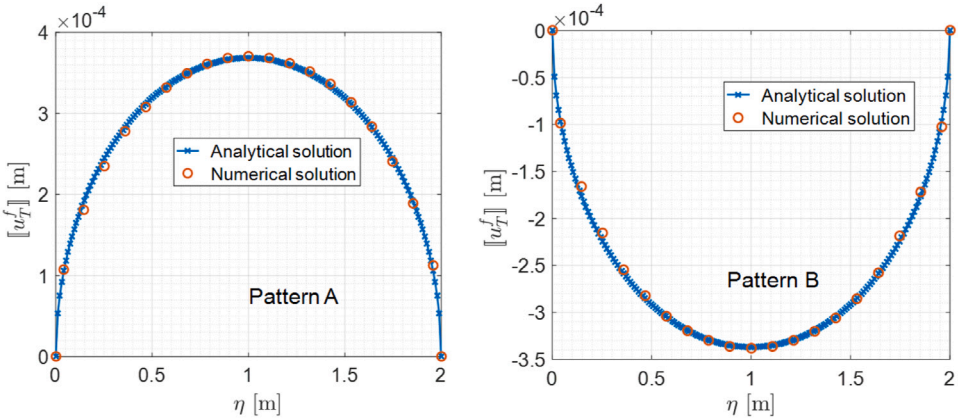

Fig. 9. The comparison of slippage between analytical and numerical solutions of the single inclined fracture.

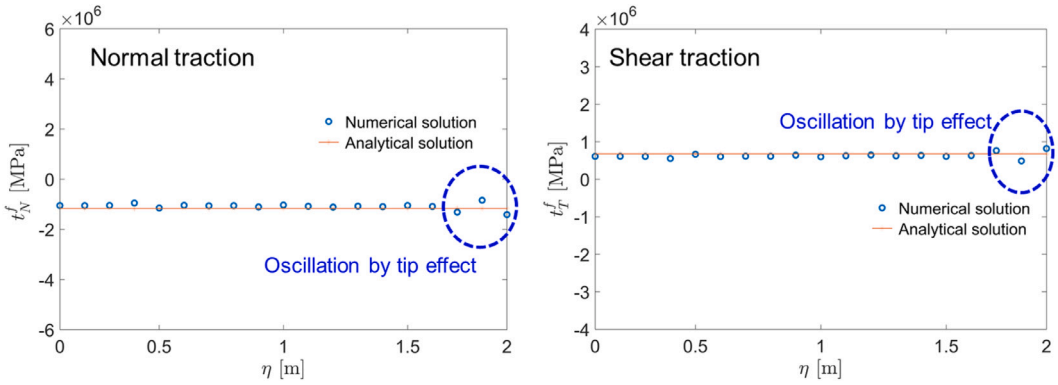

Fig. 10. Comparison of contact tractions (normal and tangential components) between analytical and numerical solutions of the single inclined fracture in Pattern A.

Fig. 9 illustrates the comparison between the analytical and numerical solutions. As shown in this figure, the relative displacement (slippage) on contact surface shows a "parabolic" shape. Furthermore, the tangential component of relative displacement on contact surface is calculated in case of Pattern B, as shown in Fig. 9. The results imply that the numerical solutions are consistent with the analytical results. Fig. 10 indicates the components of traction maintain constant. The analytical and numerical results agree well with each other. Moreover, the slight oscillation on the crack tip is observed at the endpoint of x-coordinate, as well as along the fracture. It is a common observation reported in literature. Typically, some of the methods developed in the literature (e.g., Fig. 8 in [4] and Fig. 17 in [53]) have also observed an oscillatory pattern in the variation of normal traction along the contact surface.

In addition, the slip profile long the fracture obtained by the finite volume method (e.g., Fig. 12 in [26]) and the penalty method (e.g., Fig. 8 in [4]) displays a relative larger error compared with the result calculated by our method (Fig. 9). More precisely, Fig. 11

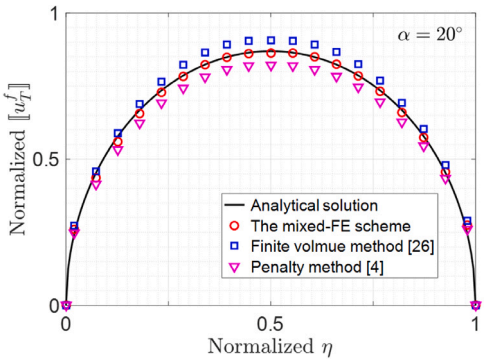

Fig. 11. Comparison of the normalized slippage along fracture calculated by different methods. The results of finite volume and penalty methods are extracted from [4,26], respectively.

provides a detailed comparison of the slip profile calculated by different methods for this test case. Note that the results of finite volume and penalty methods are extracted from [4,26], respectively. From this figure, it is clear that the presented mixed-FE scheme outperforms both the finite volume and the penalty methods.

To study the grid convergence of our method, we analyze the convergence performance with the grid refinement. The size of the domain is $10\ \text{m} \times 10\ \text{m}$. The local refinement is applied close to the inclined fracture, while the coarse grids are used far from the fracture. The grid resolution on the fracture surface is h_{min}, while the grid resolution on the edges of this domain is h_{max}. Then, h_{min} is set to be changed at a fixed h_{max}. We set $h_{min} = 0.05 \sim 0.15$ with the step of 0.02, while the coarse resolution h_{max} is set to 0.5 and 1. Fig. 12a provides several examples of grid refinements. The error ϵ_h is defined as:

$$\epsilon_h = \sum_{i=1}^{n_{cp}} \frac{\left\| x_i^{ref} - x_i^h \right\|_2}{\left\| x_i^{ref} \right\|_2} \tag{29}$$

where n_{cp} is the number of contact pairs on fracture surface. x_i^{ref} is the reference solution.

The results calculated by different grid resolutions, denoted as x_i^h, are compared with the reference solution. Note that x_i can be the slippage $[\![u_T^f]\!]$, normal traction t_N^f or tangential traction t_T^f on fracture surface. Convergence performance of this method, evaluated by different grid refinements, is displayed in Fig. 12b. It proves that the error, also implying the oscillation shown in Fig. 10, may decrease with the grid refinement. Note that the decrease of oscillation is a relative results. It means that we will obtain a relatively small oscillation with the refinement. But if we zoom in the local segment of the curves, the slight oscillation still exists, as reported in literature [4,53].

The importance of considering contact behavior is depicted in Fig. 13. As illustrated in the enlarged view, the grids on two sides of contact surface would be penetrated to each other if contact constraints are neglected. In contrast, a pair of contact traction corresponding to the two sides would be naturally created in the framework of Lagrange multiplier method to prevent the penetration when considering contact effect on fracture.

5.2. Shear failure on fracture surface

A fractured medium, which is intersected by a single fracture crossing the entire domain, is used to analyze the pure sliding along the fracture surface. We follow the same parameters as the benchmark provided in literature [55]. The material properties of elastic material are $E = 5$ GPa and $\nu = 0.3$. The frictional angle $\varphi = 5.71°$ (means the frictional coefficient is $\tan\varphi \approx 0.1$) and cohesion $c = 0$.

Two different patterns (Patterns A and B) of this model are simulated. The fracture partially intersects this domain in Pattern A. The coordinates of fracture are shown in Fig. 14. The crack tips are no longer surrounded by the host elastic matrix, thus deformation contour shows a different pattern compared with the case of embedded fracture model (for instance the model in Section 5.1), as displayed in Fig. 14. The upper part of the geometry has a significant movement, such that the entire body slips along the fracture surface. Fig. 15a shows a comparison of results calculated by the presented method and the reference solution.

As a comparison, Pattern B of this model is analyzed, as discussed in [53]. In this pattern, the deformable domain is entirely intersected by the fracture, while the slippage on fracture is different from that of Pattern A. The analytical solution of slippage is a constant $\Delta u \approx 0.1414$ m according to the literature [53,55]. Fig. 15b illustrates that the numerical solution agrees well with the analytical solution.

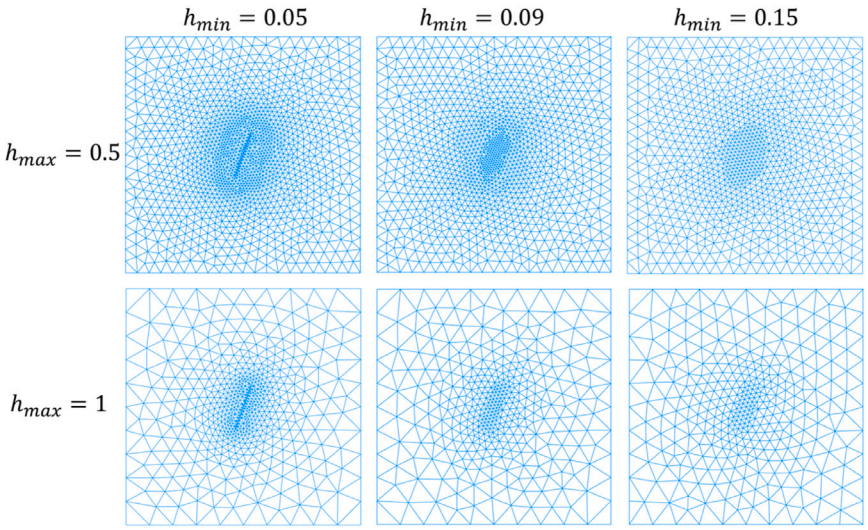

(a) Different patterns of grid refinement

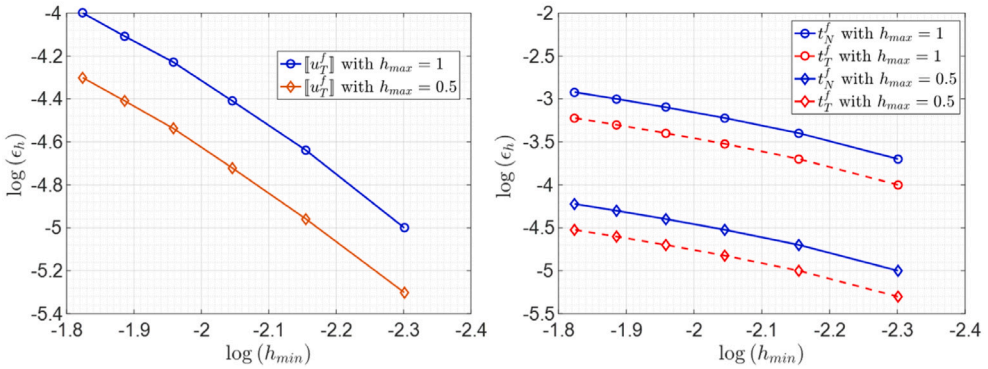

(b) Convergence performance with grid refinement

Fig. 12. Grid convergence with different grid resolutions. h_{min} and h_{max} are the grid resolutions on fracture surface and on the model edges, respectively.

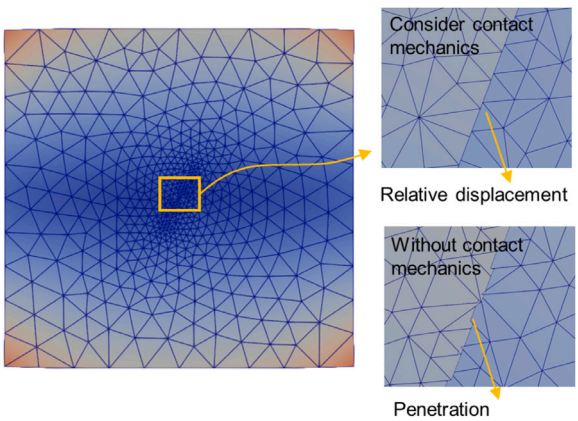

Fig. 13. Deformation of finite element grids. The numerical treatment of frictional contact and sliding prevents the penetration of grid on fracture surfaces.

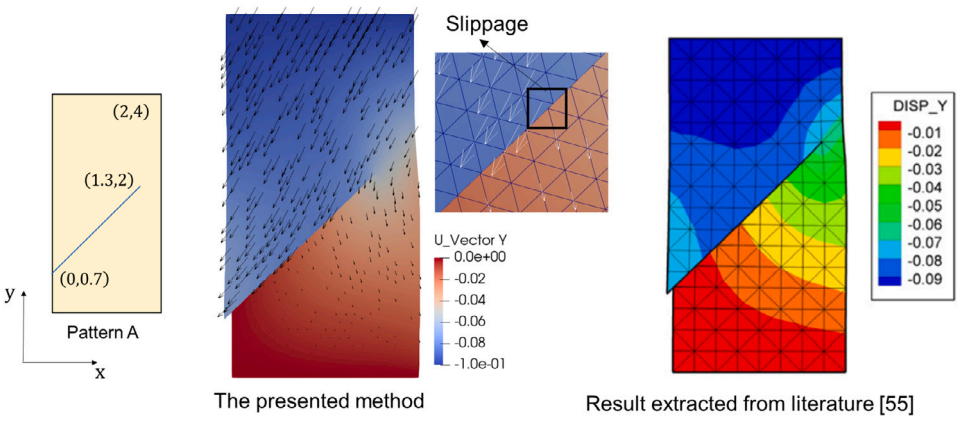

Fig. 14. Deformation of fracture sliding in Pattern A. The slippage of contact surface is measured by the tangential displacement.

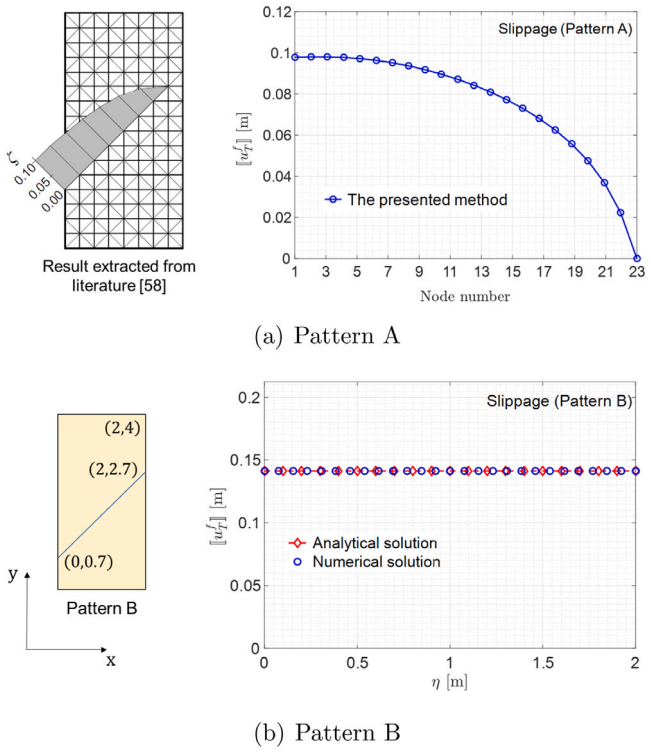

Fig. 15. The comparison between numerical solutions and reference solutions.

5.3. The effect of mixed-mode loadings and fluid pressure

Different types of loading mode would lead to various responses of a deformable fractured medium. The preceding tests focus on pure uniaxial compression or single type of loading instead of mixed-mode loading conditions. In this section, a fractured medium, with the same geometry shown in Fig. 8, is studied. In contrast to that, the compressive+shear mode (Pattern A) and the tensile+shear mode (Pattern B) are considered. $E = 50$ GPa and $\varphi = 30°$. The normal stress equals 10 MPa on the top surface of the model, while the shear stress allows varied $5 \sim 8$ MPa. It is obvious that the contact constraints would be active if Pattern A is applied. While the situation shows a distinct in Pattern B, in which the two sides of fracture surface would be separate thus the contact constraints are no longer active.

Fig. 16 shows the characteristics of displacement along the off-diagonal of the domain and provides a comparison between Pattern A and Pattern B. Note that the jump of displacement at the position, which is intersected by the fracture, exhibits different

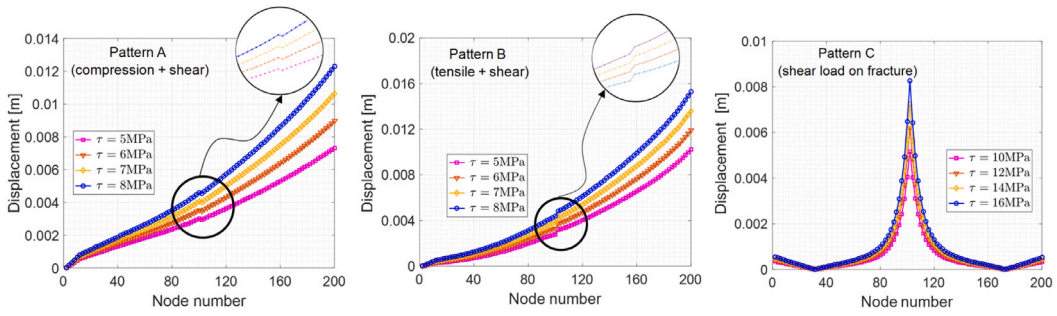

Fig. 16. Variation of displacement across the contact surface in Pattern A (left), Pattern B (middle) and Pattern C (right).

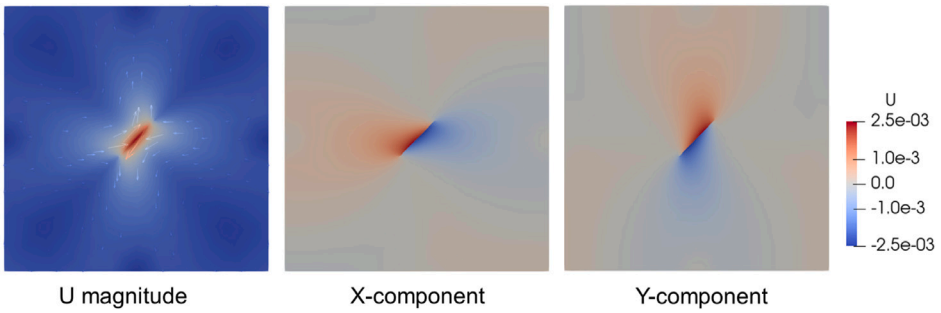

Fig. 17. Deformation in Pattern C. The imposed shear loading on contact surface leads to the symmetric mode of displacement.

features as shown in the enlarged views. Furthermore, the increased value of shear loading leads to the corresponding increased displacement magnitude on fracture.

Pattern C is designed to analyze the shear behavior on contact surface. Fig. 17 shows the deformation profile if fracture surface is imposed by an inverse pair of traction on the corresponding two sides of fracture surface. The range of shear stress is $10 \sim 16$ MPa. It can be seen from this figure that the shear loading produces a symmetric distribution of displacement field along the diagonal line in the domain. A monitoring line is placed along the off-diagonal line in the domain to measure the variation of displacement. Fig. 16 captures a sharp shift of displacement magnitude on the fracture.

The scenario is different when the internal fluid pressure is considered. As displayed in Fig. 18, the fractured surface is imposed by internal pressure which is normal to the two sides of fracture, and their directions are opposite to each other. In this way, one can model the scenario of fluid pressure in a hydro-mechanical process. The displacement vector field in Fig. 18 illustrates the opening of fracture surface. Especially, the discontinuous phenomenon generated by the opened surface can be calculated by an analytical solution from literature [26,56]:

$$\Delta u = \frac{2lp(1-\nu)}{G}\sqrt{1-\left(\frac{\eta}{l}\right)^2} \tag{30}$$

with the applied fluid pressure $p = 10$ MPa and coordinate η on contact surface. $l = 1$ m is the half length of the fracture, as shown in Fig. 8. G is the shear modulus of the elastic host matrix.

Fig. 18 shows the deformation pattern is symmetric along the off-diagonal line across the entire domain. The components of the up and down sides of the fracture surface illustrate the deformation distribution jumps by the sharp region that intersected by fracture. The enlarged view of the fracture provides an observation to show the opening and displacement vector field. Fig. 19 shows a comparison between analytical and numerical solutions. The shape of opening curve is "parabolic" which is same as the curve of slippage in compressive loading (Fig. 9).

5.4. Crossing fractures under mixed-mode loadings

The simulation of frictional contact and shear failure on crossing fractures raises several challenges in computational mechanics [13,57]. The capability of modeling frictional contact and sliding on multiple crossing fractures is one of the innovations of the presented work, as discussed in Sections 2 and 3.

A complex fractured medium is simulated to show the contact behavior of fractured media containing crossing fractures, as shown in Fig. 20. The parameters are same as the above case.

The crossing contact pairs are defined in Section 3.3 to resolved the contact mechanics at the intersected position. The deformation profile, when the compressive loading is applied, is shown in Fig. 21a. The interaction of multiple fractures at the

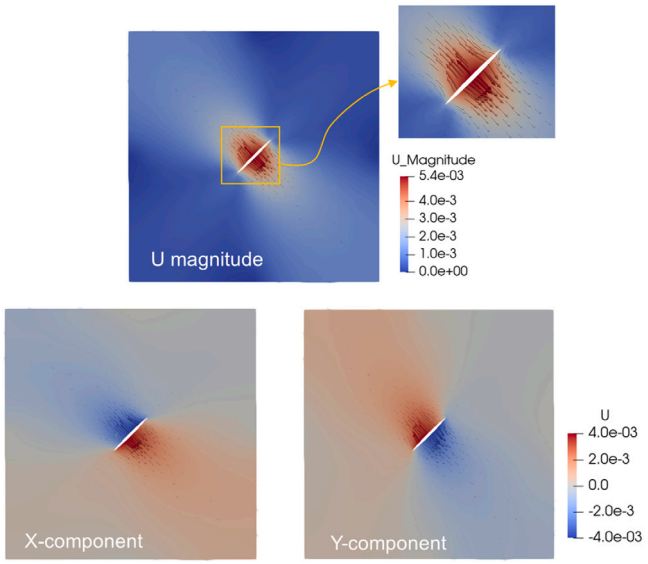

Fig. 18. Deformation contours when fluid pressure applied on fracture plane. Note that the deformation is amplified by 10 times for visualization.

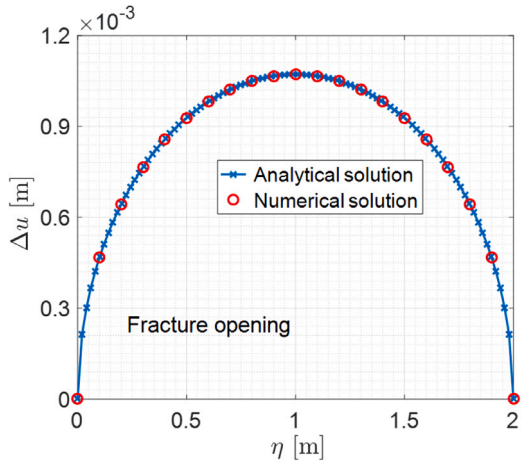

Fig. 19. The comparison of fracture opening between analytical and numerical solutions when fluid pressure imposed on the fracture.

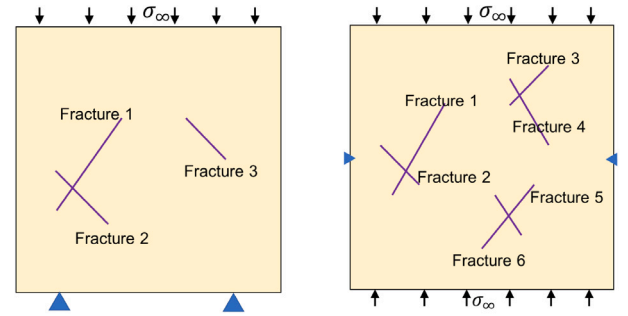

(a) Single-crossed fractures model (b) Multiple-crossed fractures model

Fig. 20. Schematics of numerical model with different fracture patterns.

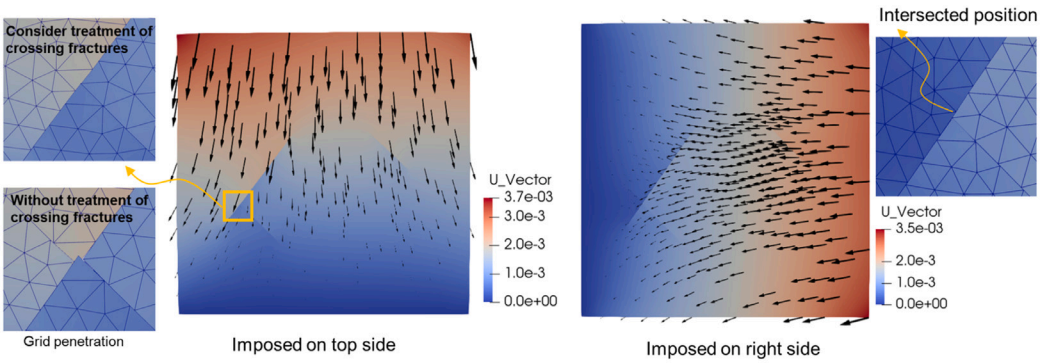

(a) Compressive loading

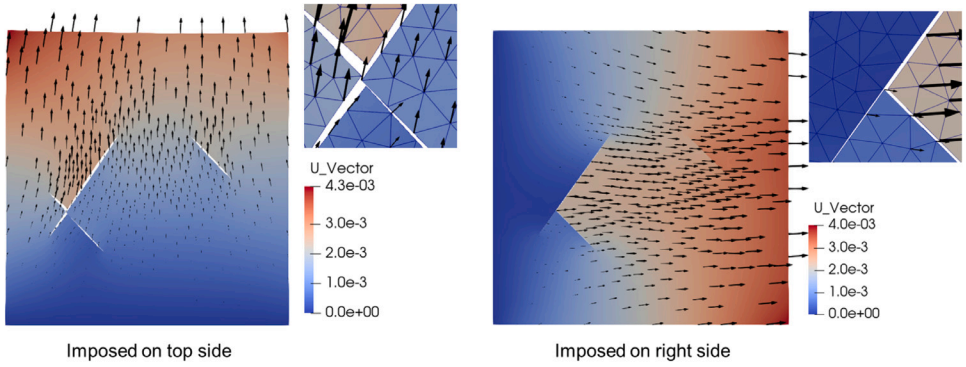

(b) Tensile loading

Fig. 21. Displacement of the single-crossed fractures model. Note that the deformation is amplified by 50 times for visualization.

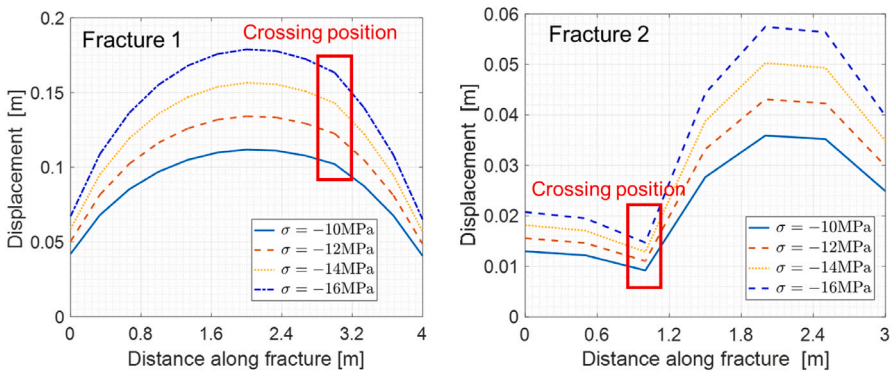

Fig. 22. The slippage on fracture surfaces in the single-crossed fractures model under compression (imposed on the top side).

crossing position can be observed in the enlarged views. In this figure, a comparison shown in the enlarged insets is provided to demonstrate the effect of treatment of crossing fractures on contact behavior. The displacement vector illustrates the influence of the existing contact surfaces, where a direction shift of the displacement vector is observed around the fractures. Moreover, the treatment of crossing fractures is important to the numerical simulation. Otherwise, a mesh penetration would be occurred at the position of crossing fractures.

Fig. 22 depicts the variations of slippage on Fractures 1 and 2, which are labeled in Fig. 20a. The crossing positions is marked by a box in this figure. If the compressive loading is applied, as shown in Fig. 21a, with an increased stress, the value of slippage would be increased as well. However, the curves of Fractures 1 and 2 show different features. It can be observed that the slippage on Fracture 1 is greater than that of Fracture 2 due to the effect of intersected fractures. The shape of slippage curve shown in Fig. 22a is parabolic and is comparable with the shape illustrated in Fig. 9.

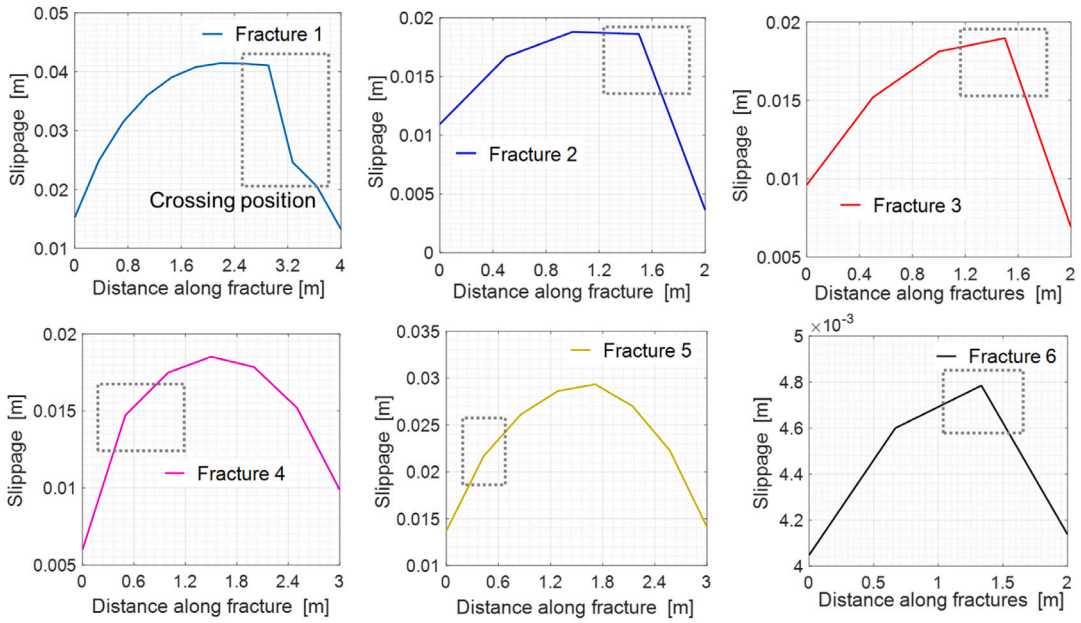

Fig. 23. Fracture slippage of the multiple-crossed fractures model. Note that the portions marked by dashed boxes imply the crossing positions. Fracture numbers are labeled in Fig. 20.

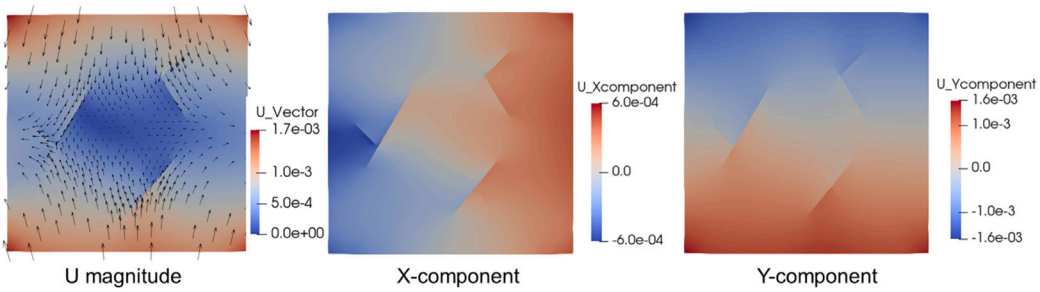

Fig. 24. Deformation of the multiple-crossed fractures model. The vector field (left) and the displacement components (middle and right).

As a contrast comparison study, a tensile loading is applied to analyze the opening on fracture surface. This distinct can be classified by the vector arrows in Fig. 21. In addition, the opening at the crossing position is observed and shown by the amplified view, which demonstrates a desirable capability of the proposed numerical scheme to simulate the opening of crossing fractures.

The schematic of a medium with multiple crossing fractures is displayed in Fig. 20b. A set of multiple crossing fractures is simulated in this test. The simulation results show the stability of the proposed numerical method when multiple crossing fractures are considered. The displacement field is shown in Fig. 24. It appears that the displacement vector arrows have some shifts around the fractures. Fig. 23 shows the slippage on each fracture in the fractured domain. The number of fractures is labeled in Fig. 20b. The shape of each curve is similar to the curve in the test of single-fractured model, i.e. the parabolic mode, as discussed in Section 5.1. A characteristic among these six fractures is the jump displacement at the crossing positions produced by the intersected fractures.

Fig. 25 displays the relation of the normalized stress intensity factor (SIF) ratio versus the loading ratio. Concerning the pure mode I or mode II, the SIFs are K_I and K_{II}, respectively. The normalized SIF ratio is commonly used to evaluate the domination of mode I and mode II fracture [58]. It is defined as $(2/\pi)\arctan(K_I/K_{II})$. We test two different mixed-mode loadings, which are the compression or shear loading combines the fluid pressure imposed on internal surface of fractures. It appears that the fluid pressure induces a larger opening of fractures, also know as the mode I failure. In contrast, the compression and shear loadings lead to a shear failure (mode II). With the increase of σ or τ, the normalized SIF ratio shows a decrease tendency. The shear failure mode becomes the domination compared to fracture opening (tensile failure, mode I), especially when the loading ratios $|\sigma/p|$ and τ/p are greater than 1.

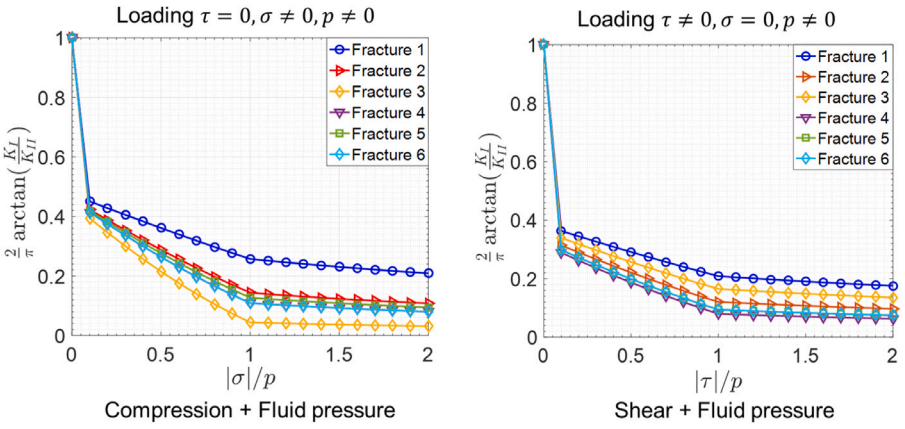

Fig. 25. Variation of the normalized SIF ratio under mixed-mode loadings. Fracture numbers are labeled in Fig. 20.

6. Conclusions

In this work, a stabilized mixed-FE scheme is proposed using the Lagrange multiplier method in the framework of constrained variational principle, which has the capability to simulate frictional contact and shear failure of multiple crossing fractures under mixed-mode loadings. The additional constraints of frictional contact are integrated into the variational principle through Lagrange multipliers. Compressive loading would lead to the activation of contact constraints, while the tensile loading remains the standard scheme of elasticity.

Galerkin finite element method is used to discretize the governing equations. Next, a novel treatment is devised to overcome the unphysical scenario at the crossing position. The preconditioning technique is introduced to preserve the robustness of the saddle-point algebraic system, which leads to a stabilized mixed-FE formulation. Then, the system is resolved using the monolithic iteration strategy, motivated by the high nonlinear property of the governing equations. The displacement and Lagrange multiplier are calculated simultaneously in one algebraic system.

A series of numerical tests is conducted to study the frictional contact and slip of single fracture and multiple crossing fractures based on the proposed mixed-FE scheme. First, a benchmark study is presented to verify the numerical results. Later, the contact behavior of fractures is analyzed under mixed-mode loading. The internal fluid pressure on fracture surface is considered. A deformable medium with multiple fractures is simulated. Especially, the effect of crossing fractures can be observed in the simulation. The characteristics of fracture contact, surface sliding (mode II), opening (mode I) and variation of SIF are analyzed. The potential diagonal contact, at the intersected position of crossing fractures, is studied under different mixed-mode loading types. The impact of intersected fractures on frictional contact is analyzed. The results prove that mode II SIF will increase if the external compressive loading increases as well, while the decrease of internal fluid pressure induces a decreased model I SIF. The curve of slippage induced by compression, as well as the opening induced by internal fluid pressure, along fracture is parabolic shape.

CRediT authorship contribution statement

Luyu Wang: Software, Methodology, Formal analysis, Conceptualization, Writing – original draft. **Cornelis Vuik:** Supervision, Writing – review & editing. **Hadi Hajibeygi:** Writing – review & editing, Supervision, Funding acquisition, Conceptualization.

Declaration of competing interest

The authors declare that they have no known competing financial interests or personal relationships that could have appeared to influence the work reported in this paper.

Acknowledgments

Financial support of NWO-TTW ViDi grant (project ADMIRE 17509) is acknowledged. Luyu Wang gratefully acknowledges the financial support by China Scholarship Council (No. 201904910310). The authors would like to thank all the members of the DARSim (Delft Advanced Reservoir Simulation) research group and ADMIRE project members at TU Delft, for the fruitful discussions.

Appendix A. Weak forms derived by the constrained variational principle

Following the formulation in Section 3, we have the weak form if the fractures are stick:

$$\delta \Pi_u^{CL}\left(\mathbf{u}^f,\lambda\right)=\sum_{i=1}^{N^f}\int_{\Gamma_{in,i}}\lambda^T\delta\mathbf{C}\left(\mathbf{u}^f,\mathbf{t}^f\right)d\Gamma=\sum_{i=1}^{N^f}\int_{\Gamma_{in,i}}\delta[\![\hat{\mathbf{u}}^f]\!]^T\lambda d\Gamma \tag{A.1}$$

with the relative displacement vector $[\![\hat{\mathbf{u}}^f]\!]=[[\![u_N^f]\!]\ \ [\![u_T^f]\!]]^T$ in the local coordinate system attached to a certain fracture surface $\Gamma_{in,i}$, as shown in Fig. 3. Meanwhile, Eq. (15) is written as:

$$\delta \Pi_\lambda^{CL}\left(\mathbf{u}^f,\lambda\right)=\sum_{i=1}^{N^f}\int_{\Gamma_{in,i}}\delta\lambda^T\mathbf{C}\left(\mathbf{u}^f,\mathbf{t}^f\right)d\Gamma=\sum_{i=1}^{N^f}\int_{\Gamma_{in,i}}\delta\lambda^T\left([\![\hat{\mathbf{u}}^f]\!]+\mathbf{g}\right)d\Gamma \tag{A.2}$$

with the initial gap $\mathbf{g}=[g_N\ \ 0]^T$ between + side and — side, as indicated in Eq. (9). Normally, g_N equals either 0 or a small value such as $10^{-3}\sim10^{-4}$ m.

Following the minimization of energy functional [59,60], the constrained variational principle with Lagrange multiplier requires:

$$\begin{aligned}\int_\Omega\delta\boldsymbol{\varepsilon}^T\boldsymbol{\sigma}d\Omega-\int_\Omega\delta\mathbf{u}^T\mathbf{f}d\Omega-\int_{\Gamma_{ex}^N}\delta\mathbf{u}^T\bar{\mathbf{t}}^{ex}d\Gamma+\sum_{i=1}^{N^f}\int_{\Gamma_{in,i}}\delta[\![\hat{\mathbf{u}}^f]\!]^T\lambda d\Gamma=0\\ \sum_{i=1}^{N^f}\int_{\Gamma_{in,i}}\delta\lambda^T[\![\hat{\mathbf{u}}^f]\!]d\Gamma=-\sum_{i=1}^{N^f}\int_{\Gamma_{in,i}}\delta\lambda^T\mathbf{g}d\Gamma\end{aligned} \tag{A.3}$$

The two equations in system Eq. (A.3) are independent to each other. We calculate the unknowns, displacement $\mathbf{u}$ and Lagrange multiplier λ, in a framework of numerical scheme, namely the mixed-FE scheme.

In the situation of fracture sliding, the first-order variation of energy functional with respect to displacement is given by:

$$\begin{aligned}\int_\Omega\delta\boldsymbol{\varepsilon}^T\boldsymbol{\sigma}d\Omega-\int_\Omega\delta\mathbf{u}^T\mathbf{f}d\Omega-\int_{\Gamma_{ex}^N}\delta\mathbf{u}^T\bar{\mathbf{t}}^{ex}d\Gamma+\sum_{i=1}^{N^f}\left(\int_{\Gamma_{in,i}}[\![\delta u_N^f]\!]\lambda_N d\Gamma\right.\\ \left.+\int_{\Gamma_{in,i}}[\![\delta u_T^f]\!]c\ signd\Gamma-\int_{\Gamma_{in,i}}[\![\delta u_T^f]\!]\lambda_N sign\tan\varphi d\Gamma\right)=0\end{aligned} \tag{A.4}$$

and the variation with respect to Lagrange multiplier is given by:

$$\sum_{i=1}^{N^f}\int_{\Gamma_{in,i}}\delta\lambda_N\left([\![u_N^f]\!]-[\![u_T^f]\!]sign\tan\varphi\right)d\Gamma=-\sum_{i=1}^{N^f}\int_{\Gamma_{in,i}}\delta\lambda_N g_N d\Gamma \tag{A.5}$$

which holds in the scenario of multiple fractures indicated by the number of fractures N^f. Other notations are defined in the preceding sections.

Eqs. (A.3), (A.4) and (A.5) provide a general formulation which captures the frictional contact and slip of multiple fractures in deformable media under compressive, tensile and shear loadings.

Appendix B. Discretized forms of the mixed-FE scheme

Following the formulation in Section 4, the components in Eq. (25) are expressed as:

$$\begin{aligned}\mathbf{R}^u&=\mathbf{K}^{uu}\mathbf{U}+\mathbf{C}^{\lambda u}\boldsymbol{\Lambda}-\left(\mathbf{F}-\mathbf{F}^{slip}\right)\\ \mathbf{R}^\lambda&=\left[\mathbf{C}^{\lambda u}\right]^T\mathbf{U}+\mathbf{g}\\ \mathbf{C}^{\lambda u}&=\mathbf{K}^{\lambda u}+\left(\mathbf{K}^{\lambda u,N}-\mathbf{K}^{\lambda u,T}\right)\end{aligned} \tag{B.1}$$

and the sub-blocks:

$$\begin{aligned}\mathbf{K}^{uu}&=\int_\Omega\mathbf{B}^T\mathbf{D}\mathbf{B}d\Omega\\ \mathbf{K}^{\lambda u}&=\int_{\Gamma_{in}^{stick}\cup\Gamma_{in}^{slip}}\mathbf{G}^T\mathbf{S}\mathbf{N}^\lambda d\Gamma\\ \mathbf{K}^{\lambda u,N}&=\int_{\Gamma_{in}^{slip}}\mathbf{G}^T\mathbf{n}^f\mathbf{N}_N^\lambda d\Gamma\\ \mathbf{K}^{\lambda u,T}&=\int_{\Gamma_{in}^{slip}}\mathbf{G}^T\mathbf{m}^f\mathbf{N}_N^\lambda sign\tan\varphi d\Gamma\\ \mathbf{F}&=\int_\Omega\left[\mathbf{N}^u\right]^T\mathbf{f}d\Omega+\int_{\Gamma_{ex}^N}\left[\mathbf{N}^u\right]^T\bar{\mathbf{t}}^{ex}d\Gamma\\ \mathbf{F}^{slip}&=\int_{\Gamma_{in}^{slip}}\mathbf{G}^T\mathbf{m}^f c\ signd\Gamma\end{aligned} \tag{B.2}$$

where the blocks $\mathbf{F}^{slip}$, $\mathbf{K}^{\lambda u,N}$ and $\mathbf{K}^{\lambda u,T}$ are related to the contributions of slip contact. $\mathbf{K}^{\lambda u}$ is related to the co-effects by stick and slip states. $sign$ is defined in Eq. (16).

The system of Eqs. (25), (B.1) and (B.2) will be constructed at each iteration step. The iteration process is controlled by the termination criterion:

$$\left\|\mathbf{R}^{n+1}\right\|_2 < \epsilon \tag{B.3}$$

with a user-defined threshold ϵ. Normally, it is set to a default value 10^{-4}. All notations are defined in the preceding sections.

Eqs. (25), (B.1) and (B.2) provide one of the core contributions of the presented work, which include an unified formulation of frictional contact mechanics and shear failure analyses of multiple fractures.

Appendix C. Expanded forms of the preconditioner

Following the formulation in Section 4.2, the expanded forms are written as:

$$\mathbf{A}^2 = \begin{bmatrix} \sum_{j=1}^{n_c^E}(E_{1j})^2 & \cdots & \cdots \\ \cdots & \sum_{j=1}^{n_c^E}(E_{2j})^2 & \cdots \\ \vdots & \ddots & \vdots \\ \cdots & \cdots & \sum_{j=1}^{n_c^E}(E_{n_r^E j})^2 \end{bmatrix} \tag{C.1}$$

$$\mathbf{B}^2 = \begin{bmatrix} \sum_{j=1}^{n_c^D}(D_{1j})^2 & \cdots & \cdots \\ \cdots & \sum_{j=1}^{n_c^D}(D_{2j})^2 & \cdots \\ \vdots & \ddots & \vdots \\ \cdots & \cdots & \sum_{j=1}^{n_c^D}(D_{n_r^D j})^2 \end{bmatrix} \tag{C.2}$$

with the numbers of columns n_c^D and rows n_r^D for $\mathbf{D}$, n_c^E and n_r^E for $\mathbf{E}$. Other notations are defined in the preceding sections. This operation provides a way to improve the numerical quality of the Jacobian. It is efficient and easy to implement.

Appendix D. The monolithic-updated contact algorithm

Algorithm 1 The monolithic-updated contact algorithm on unstructured grids

1: **for** each $i \in [1, N^f]$ **do**
2: Fracture $\Gamma_{in,i}$ is determined by its coordinate (x_i, y_i)
3: Obtain the node connectivity and contact pairs on unstructured grids
4: **end for**
Enter the procedure of contact state update
5: **for** each $t \in [0, t_{max}]$ **do**
6: At time step t, calculate the current contact state of contact pairs
7: Enter the iteration process
8: **for** each $\nu \in [0, \nu_{max}]$ **do**
9: At iteration ν, construct the system Eq. (25) based on current contact state
10: Obtain the results of contact state at iteration $\nu+1$, as indicated in Eq. (23)
11: Update the unknowns $\mathbf{U}^{\nu+1} = \mathbf{U}^{\nu} + \delta\mathbf{U}^{\nu+1}$ and $\boldsymbol{\Lambda}^{\nu+1} = \boldsymbol{\Lambda}^{\nu} + \delta\boldsymbol{\Lambda}^{\nu+1}$
12: **end for**
13: If the contact state is satisfied with contact constraints then go to the updated time step $t = t+1$, and refer to Line 6
14: Otherwise, go to Line 9 until the calculated contact state is satisfied with contact constraints
15: **if** $t = t_{max}$ **then**
16: Terminate the program
17: **end if**
18: **end for**

References

[1] Barber JR, Ciavarella M. Contact mechanics. Int J Solids Struct 2000;37:29–43. http://dx.doi.org/10.1016/S0020-7683(99)00075-X.

[2] De Lorenzis L, Wriggers P, Weißenfels C. Computational contact mechanics with the finite element method. In: Encycl comput mech. 2nd ed.. John Wiley & Sons; 2017, http://dx.doi.org/10.1002/9781119176817.ecm2033.

[3] Jha B, Juanes R. Coupled multiphase flow and poromechanics: A computational model of pore pressure effects on fault slip and earthquake triggering. Water Resour Res 2014;50:3776–808. http://dx.doi.org/10.1002/2013WR015175.

[4] Garipov TT, Karimi-Fard M, Tchelepi HA. Discrete fracture model for coupled flow and geomechanics. Comput Geosci 2016;20:149–60. http://dx.doi.org/10.1007/s10596-015-9554-z.

[5] Aagaard BT, Knepley MG, Williams CA. A domain decomposition approach to implementing fault slip in finite-element models of quasi-static and dynamic crustal deformation. J Geophys Res Solid Earth 2013;118:3059–79. http://dx.doi.org/10.1002/jgrb.50217.

[6] Wang L, Chen W, Tan X, Tan X, Yang J, Yang D, et al. Numerical investigation on the stability of deforming fractured rocks using discrete fracture networks: a case study of underground excavation. Bull Eng Geol Environ 2020;79:133–51. http://dx.doi.org/10.1007/s10064-019-01536-9.

[7] Wang L, Chen W, Vuik C. Hybrid-dimensional modeling for fluid flow in heterogeneous porous media using dual fracture-pore model with flux interaction of fracture-cavity network. J Nat Gas Sci Eng 2022;104450. http://dx.doi.org/10.1016/j.jngse.2022.104450.

[8] Zhai M, Wang D, Zhang Z, Zhang L, Yang F, Huang B, et al. Numerical simulation and multi-factor optimization of hydraulic fracturing in deep naturally fractured sandstones based on response surface method. Eng Fract Mech 2022;259:108110. http://dx.doi.org/10.1016/j.engfracmech.2021.108110.

[9] Tan X, Chen W, Wang L, Yang J, Tan X. Settlement behaviors investigation for underwater tunnel considering the impacts of fractured medium and water pressure. Mar Georesour Geotechnol 2021;39(6):639–48. http://dx.doi.org/10.1080/1064119X.2020.1737279.

[10] Wang L, Chen W, Tan X, Tan X, Yuan J, Liu Q. Evaluation of mountain slope stability considering the impact of geological interfaces using discrete fractures model. J Mt Sci 2019;16:2184–202. http://dx.doi.org/10.1007/s11629-019-5527-3.

[11] Dehghan AN. An experimental investigation into the influence of pre-existing natural fracture on the behavior and length of propagating hydraulic fracture. Eng Fract Mech 2020;240:107330. http://dx.doi.org/10.1016/j.engfracmech.2020.107330.

[12] Parchei-Esfahani M, Gee B, Gracie R. Dynamic hydraulic stimulation and fracturing from a wellbore using pressure pulsing. Eng Fract Mech 2020;235:107152. http://dx.doi.org/10.1016/j.engfracmech.2020.107152.

[13] Annavarapu C, Hautefeuille M, Dolbow JE. A nitsche stabilized finite element method for frictional sliding on embedded interfaces, part II: intersecting interfaces. Comput Methods Appl Mech Eng 2013;267:318–41. http://dx.doi.org/10.1016/j.cma.2013.08.008.

[14] Sofonea M, Matei A. Mathematical models in contact mechanics. London mathematical society lecture note series, Cambridge University Press; 2012, http://dx.doi.org/10.1017/cbo9781139104166.

[15] Wriggers P. Computational contact mechanics. Springer-Verlag Berlin Heidelberg; 2006, http://dx.doi.org/10.1007/978-3-540-32609-0.

[16] Yastrebov VA, Breitkopf P. Numerical methods in contact mechanics. John Wiley & Sons; 2013, http://dx.doi.org/10.1002/9781118647974.

[17] Zhong ZH. Finite element procedures for contact-impact problems. Oxford science publications; 1993.

[18] Franceschini A, Ferronato M, Janna C, Teatini P. A novel Lagrangian approach for the stable numerical simulation of fault and fracture mechanics. J Comput Phys 2016;314:503–21. http://dx.doi.org/10.1016/j.jcp.2016.03.032.

[19] Zhao X, Jha B. A new coupled multiphase flow–finite strain deformation–fault slip framework for induced seismicity. J Comput Phys 2021;433(15):110178. http://dx.doi.org/10.1016/j.jcp.2021.110178.

[20] Peshcherenko A, Chuprakov D. An ultrafast simulator for 3D propagation of a hydraulic fracture with rectangular shape. Eng Fract Mech 243:107512. http://dx.doi.org/10.1016/j.engfracmech.2020.107512.

[21] HosseiniMehr M, Tomala JP, Vuik C, Al Kobaisi M, Hajibeygi H. Projection-based embedded discrete fracture model (pEDFM) for flow and heat transfer in real-field geological formations with hexahedral corner-point grids. Adv Water Resour 2022;159:104091. http://dx.doi.org/10.1016/j.advwatres.2021.104091.

[22] Liu F, Borja RI. Stabilized low-order finite elements for frictional contact with the extended finite element method. Comput Methods Appl Mech Engrg 2010;199:2456–71. http://dx.doi.org/10.1016/j.cma.2010.03.030.

[23] Liu F, Borja RI. A contact algorithm for frictional crack propagation with the extended finite element method. Int J Numer Methods Eng 2008;76:1489–512. http://dx.doi.org/10.1002/nme.2376.

[24] Xu F, Hajibeygi H, Sluys LJ. Multiscale extended finite element method for deformable fractured porous media. J Comput Phys 2021;436:110287. http://dx.doi.org/10.1016/j.jcp.2021.110287.

[25] Berge RL, Berre I, Keilegavlen E, Nordbotten JM, Wohlmuth B. Finite volume discretization for poroelastic media with fractures modeled by contact mechanics. Int J Numer Methods Eng 2020;121:644–63. http://dx.doi.org/10.1002/nme.6238.

[26] Ucar E, Keilegavlen E, Berre I, Nordbotten JM. A finite-volume discretization for deformation of fractured media. Comput Geosci 2018;22:993–1007. http://dx.doi.org/10.1007/s10596-018-9734-8.

[27] Deb R, Jenny P. Modeling of shear failure in fractured reservoirs with a porous matrix. Comput Geosci 2017;5:1119–34. http://dx.doi.org/10.1007/s10596-017-9680-x.

[28] Mergheim J, Kuhl E, Steinmann P. A hybrid discontinuous Galerkin/interface method for the computational modelling of failure. Commun Numer Methods Eng 2004;20:511–9. http://dx.doi.org/10.1002/cnm.689.

[29] Ferronato M, Gambolati G, Janna C, Teatini P. Numerical modelling of regional faults in land subsidence prediction above gas/oil reservoirs. Int J Numer Anal Methods Geomech 2008;32:633–57. http://dx.doi.org/10.1002/nag.640.

[30] Pietrzak G, Curnier A. Large deformation frictional contact mechanics: Continuum formulation and augmented Lagrangian treatment. Comput Methods Appl Mech Engrg 1999;177:351–81. http://dx.doi.org/10.1016/S0045-7825(98)00388-0.

[31] Simo JC, Laursen TA. An augmented lagrangian treatment of contact problems involving friction. Comput Struct 1992;42:97–116. http://dx.doi.org/10.1016/0045-7949(92)90540-G.

[32] Sokolova I, Bastisya MG, Hajibeygi H. Multiscale finite volume method for finite-volume-based simulation of poroelasticity. J Comput Phys 2019;379:324–79. http://dx.doi.org/10.1016/j.jcp.2018.11.039.

[33] Simo JC, Wriggers P, Taylor RL. A perturbed Lagrangian formulation for the finite element solution of contact problems. Comput Methods Appl Mech Engrg 1985;50:163–80. http://dx.doi.org/10.1016/0045-7825(85)90088-X.

[34] Franceschini A, Castelletto N, Ferronato M. Block preconditioning for fault/fracture mechanics saddle-point problems. Comput Methods Appl Mech Engrg 2019;344:376–401. http://dx.doi.org/10.1016/j.cma.2018.09.039.

[35] Auricchio F, da Veiga LB, Brezzi F, Lovadina C. Mixed finite element methods. In: Encycl comput mech. 2nd ed.. John Wiley & Sons; 2017, http://dx.doi.org/10.1002/9781119176817.ecm2004.

[36] Pestana J, Wathen AJ. Natural preconditioning and iterative methods for saddle point systems. SIAM Rev 2015;57:71–91. http://dx.doi.org/10.1137/130934921.

[37] Cescotto S, Charlier R. Frictional contact finite elements based on mixed variational principles. Int J Numer Methods Eng 1993;36:1681–701. http://dx.doi.org/10.1002/nme.1620361005.

[38] Hansbo P. Nitsche's method for interface problems in computational mechanics. GAMM-Mitt 2005;28:183–206. http://dx.doi.org/10.1002/gamm.201490018.

[39] Annavarapu C, Hautefeuille M, Dolbow JE. A robust nitsche's formulation for interface problems. Comput Methods Appl Mech Engrg 2012;225(228):44–54. http://dx.doi.org/10.1016/j.cma.2012.03.008.

[40] Nejati M, Paluszny A, Zimmerman RW. A finite element framework for modeling internal frictional contact in three-dimensional fractured media using unstructured tetrahedral meshes. Comput Methods Appl Mech Engrg 2016;306:123–50. http://dx.doi.org/10.1016/j.cma.2016.03.028.

[41] Farah P, Popp A, Wall WA. Segment-based vs. Element-based integration for mortar methods in computational contact mechanics. Comput Mech 2015;55:209–28. http://dx.doi.org/10.1007/s00466-014-1093-2.

[42] Seitz A, Farah P, Kremheller J, Wohlmuth BI, Wall WA, Popp A. Isogeometric dual mortar methods for computational contact mechanics. Comput Methods Appl Mech Engrg 2016;301:259–80. http://dx.doi.org/10.1016/j.cma.2015.12.018.

[43] Garipov TT, Hui MH. Discrete fracture modeling approach for simulating coupled thermo-hydro-mechanical effects in fractured reservoirs. Int J Rock Mech Min Sci 2019;122:104075. http://dx.doi.org/10.1016/j.ijrmms.2019.104075.

[44] Dang-Trung H, Keilegavlen E, Berre I. Numerical modeling of wing crack propagation accounting for fracture contact mechanics. Int J Solids Struct 2020;204:233–47. http://dx.doi.org/10.1016/j.ijsolstr.2020.08.017.

[45] Gallyamov E, Garipov T, Voskov D, Van den Hoek P. Discrete fracture model for simulating waterflooding processes under fracturing conditions. Int J Numer Anal Methods Geomech 2018;42(13):1445–70. http://dx.doi.org/10.1002/nag.2797.
[46] Dang-Trung H, Berre I, E. Keilegavlen. Multiscale simulation of injection-induced fracture slip and wing-crack propagation in poroelastic media. 2021, arXiv preprint arXiv:2112.01811.
[47] Van der Vorst HA, Vuik C. Linear algebraic solvers and eigenvalue analysis. In: Encycl comput mech. 2nd ed.. John Wiley & Sons; 2017, http://dx.doi.org/10.1002/9781119176817.ecm2016.
[48] Simo CJ, Hughes TJR. Computational inelasticity. Springer Science and Business Media; 2006, http://dx.doi.org/10.1007/b98904.
[49] Zienkiewicz OC, Taylor LR. The finite element method: solid mechanics. Butterworth-heinemann; 2000.
[50] Bertsekas DP. Constrained optimization and lagrange multiplier methods. Academic Press; 1982, http://dx.doi.org/10.1016/c2013-0-10366-2.
[51] Ito K, Kunisch K. Lagrange multiplier approach to variational problems and applications. Society for Industrial and Applied Mathematics; 2008, http://dx.doi.org/10.1137/1.9780898718614.
[52] Brenner S, Scott R. The mathematical theory of finite element methods. Springer Science and Business Media; 2007, http://dx.doi.org/10.1007/978-0-387-75934-0.
[53] Franceschini A, Castelletto N, White JA, Tchelepi HA. Algebraically stabilized Lagrange multiplier method for frictional contact mechanics with hydraulically active fractures. Comput Methods Appl Mech Engrg 2020;368:113161. http://dx.doi.org/10.1016/j.cma.2020.113161.
[54] Phan AV, Napier JAL, Gray LJ, Kaplan T. Symmetric-Galerkin BEM simulation of fracture with frictional contact. Int J Numer Methods Eng 2003;57:835–51. http://dx.doi.org/10.1002/nme.707.
[55] Borja RI. Assumed enhanced strain and the extended finite element methods: A unification of concepts. Comput Methods Appl Mech Engrg 2008;197:2789–803. http://dx.doi.org/10.1016/j.cma.2008.01.019.
[56] Sneddon IN. Fourier transforms. Courier Corporation; 1995.
[57] Stefansson I, Berre I, Keilegavlen E. A fully coupled numerical model of thermo-hydro-mechanical processes and fracture contact mechanics in porous media. Comput Methods Appl Mech Engrg 2021;386:114122. http://dx.doi.org/10.1016/j.cma.2021.114122.
[58] Wang L, Chen W, Tan X, Yang J. The impact of various crack geometrical parameters on stress field over tip under different mixed loading conditions and inclination angles. Theor Appl Fract Mech 2019;102:239–54. http://dx.doi.org/10.1016/j.tafmec.2018.12.001.
[59] Lanczos C. The variational principles of mechanics. Courier Corporation; 2012.
[60] Reddy JN. Energy principles and variational methods in applied mechanics. John Wiley & Sons; 2017.